Modeling the effect of lithium-induced pedestal profiles on scrape-off-layer turbulence and the heat flux width

D. A. Russell, D. A. D'Ippolito, J. R. Myra,
Lodestar Research Corporation, Boulder, CO, USA

J. M. Canik, T. K. Gray,
Oak Ridge National Laboratory, Oak Ridge, TN, USA

S. J. Zweben
Princeton Plasma Physics Laboratory, Princeton, NJ, USA

Modeling the effect of lithium-induced pedestal profiles on scrape-off-layer turbulence and the heat flux width

D. A. Russell,[†] D. A. D'Ippolito, J. R. Myra

Lodestar Research Corporation, 2400 Central Avenue, Boulder, CO, USA

J. M. Canik, T. K. Gray

Oak Ridge National Laboratory, Oak Ridge, TN, USA

S. J. Zweben

Princeton Plasma Physics Laboratory, Princeton, NJ, USA

Abstract

The effect of lithium (Li) wall coatings on scrape-off-layer (SOL) turbulence in the National Spherical Torus Experiment (NSTX) is modeled with the Lodestar SOLT ("SOL Turbulence") code. Specifically, the implications for the SOL heat flux width of experimentally observed, Li-induced changes in the pedestal profiles are considered. The SOLT code used in the modeling has been expanded recently to include ion temperature evolution and ion diamagnetic drift effects. This work focuses on two NSTX discharges occurring pre- and with-Li deposition. The simulation density and temperature profiles are constrained, inside the last closed flux surface only, to match those measured in the two experiments, and the resulting drift-interchange-driven turbulence is explored. The effect of Li enters the simulation only through the pedestal profile constraint: Li modifies the experimental density and temperature profiles in the pedestal, and these profiles affect the simulated SOL turbulence. The power entering the SOL measured in the experiments is matched in the simulations by adjusting "free" dissipation parameters (e.g., diffusion coefficients) that are not measured directly in the experiments. With power-matching, (a) the heat flux SOL width is smaller, as observed experimentally by infra-red thermography, and (b) the simulated density fluctuation amplitudes are reduced with Li, as inferred for the experiments as well from reflectometry analysis. The instabilities and saturation mechanisms that underlie the SOLT model equilibria are also discussed.

†email: **dave@lodestar.com**

I. Introduction

Understanding particle and heat transport in the edge and scrape-off-layer (SOL) is important because edge pedestal profiles impact the overall fusion performance of ITER and future fusion devices, while the SOL heat-flux width λ impacts the survivability of divertor target plates. One important question is whether the SOL width is set by turbulence or by neoclassical transport and how it, and the related peak power load on the divertor, can be controlled. Another issue is how wall conditioning can be exploited to improve tokamak performance. These considerations motivated the study of lithium (Li)-coated walls in the National Spherical Torus Experiment (NSTX) and the 2D turbulence modeling described in the present paper. The computed heat-flux widths in the turbulence-dominated simulations with and without Li agree qualitatively with the experiments. The results of this study imply a novel linkage between pedestal profiles and SOL profiles due to non-local turbulent transport.

It has been established that lithium (Li) wall conditioning improves tokamak performance. With lithium deposition on plasma-facing components (PFCs) in NSTX, observed improvements include increases in electron and ion temperature, increases in energy confinement times and reduced magneto-hydrodynamic turbulence[1] including the suppression of edge-localized modes (ELMs).[2] It is generally believed that a lithium coating provides improved performance through reduced ion (deuterium) recycling and better high-Z impurity control at the PFCs. However, predictive models of the interplay between plasma edge conditions and recycling dynamics are scarce, and the origins of improved confinement in lithium deposition is a topic of on-going investigation. For example, Canik et al. have postulated that changes in electron temperature gradient (ETG) and micro-tearing instabilities, driven by lithium-induced changes in the density gradient, could be responsible for ELM suppression and improved confinement, respectively.[3]

In a series of discharges in NSTX,[4,5] electron density and pressure profiles in the edge pedestal region relaxed (i.e., profile gradients decreased) significantly (~50%) with increasing lithium deposition. Along with the profile relaxation, reduced recycling, decreased electron

transport and ELM suppression were observed. ELM suppression was attributed to the reduced drive of magneto-hydrodynamic instabilities (peeling-ballooning modes) that comes with reduced pressure gradients in the edge region. A reduction in the intensity of the deuterium alpha-line emission (D_α), measured at the lower divertor in these discharges, is particularly noteworthy in the context of this paper, as it points to a possible reduction in turbulent transport across the separatrix and reduced recycling. It has been observed by infrared thermography (IRTV) that Li deposition reduces both the radial heat flux ($q_\perp$) and the heat flux width, λ, at the divertor and so, by magnetic field line mapping, reduces λ in the outboard midplane (OM) in NSTX.[6]

Interpretative transport studies[7] of two of the NSTX discharges, one with and one without lithium coated PFCs, concluded that a decrease of ~75% in the particle and energy transport coefficients, D and χ_e, was consistent with the observed profile relaxation with Li deposition. That calculation was based on a diffusive transport model inside the separatrix and did not include a contribution from turbulent convection. The same study provides evidence that lithium decreases turbulent fluctuations in the edge and SOL. Edge reflectometry measurements suggest normalized density fluctuations ($\delta n/n$) of ~10% in the pre-Li case and ~1% in the with-Li case, just inside the separatrix, with the pre-Li value approaching unity in the near-SOL. Thus further investigation of the effects of lithium on turbulent transport is well motivated.

In the present study, we model turbulent transport in these two NSTX discharges, one with and one without lithium, using a newly updated version of the SOLT code. This approach was motivated by previous successful studies of the SOL heat-flux width in low-power H-mode discharges in NSTX[8] and of an EDA H-mode in Alcator C-Mod.[9] As in those studies, we focus on the heat-flux width under the constraint of matching the power crossing the separatrix in the simulations with the neutral beam injection (NBI) power in the experiments. It is demonstrated that the observed reduction in the SOL heat-flux width corresponds to the reduction in interchange-driven turbulent transport in the model simulations, which results from the gentler edge pedestal pressure profiles associated with lithium deposition.

In addition to the SOLT modeling just discussed, there has been other recent theoretical work on turbulence simulations of the SOL width. In one study with the ESEL code,[10] numerical simulations of SOL L-mode turbulence were used to create a large database of simulation results. Then regression analysis was used to construct power-scaling laws for the characteristic decay lengths of the temperature, density and heat flux at the outer midplane. In another paper,[11] a predictive theory of the SOL width, applicable to the SOL of inner-wall limited plasmas, was developed and tested by 3D flux-driven simulations with the GBS code. Various aspects of the theory, such as saturation physics, parallel dynamics, and system size scaling, were tested and verified. Comparing SOLT with these codes, it is important to note that SOLT has finite ion temperature and ion diamagnetic physics thought to be important in H-mode discharges; given the strong sheared flows in a typical H-mode, the SOLT simulations tend to show a competition between saturation mechanisms (sheared flow vs. profile relaxation) in H-mode, whereas the GBS code shows that profile flattening is the dominant turbulent saturation mechanism in L-mode.[12] In addition to finite ion temperature equations, and the dimensionality of the various fluid codes, another important distinction is the use (or not) of the Boussinesq approximation. This somewhat questionable approximation is not employed in the present version of SOLT. Finally, going beyond fluid modeling, gyrokinetic turbulence simulations addressing the SOL heat flux width in full toroidal geometry have begun to make important contributions.[13] Thus, a number of 2D and 3D codes have proved useful in simulating the SOL width for particles and energy.

The rest of the paper is organized as follows. The newly updated SOLT model equations, which now include the self-consistent evolution of the ion pressure and ion diamagnetic drift, are described in Sec. II. Section III describes the experimental input to the SOLT simulations. This includes matching to the experimental density and temperature profiles inside the separatrix, and matching the power crossing the separatrix (P_{SOL}). The power-matched heat flux widths are the main results of this paper. Section IV discusses the mean flows observed in the simulations. Gas-puff imaging (GPI) data provides information on flow velocities in NSTX. To enable

comparison with the GPI data, in Sec. IV we introduce a structure velocity diagnostic for the simulations and demonstrate its dependence on flow damping. Section V presents a summary and our conclusions. Appendix A discusses the analytic closures used to express the parallel dynamics in terms of the variables of the 2D model. Finally, Appendix B discusses the effect of the finite-T_i terms in the model on prepared blob propagation with and without the Boussinesq approximation.

II. Model Equations

SOLT is a two-dimensional (2D) electrostatic fluid turbulence code. The code models the evolution of potential, density and temperatures (electron and ion) in a plane perpendicular to the magnetic field **B** in the outboard midplane (OM) region of the torus. The simulation plane is the (x,y) plane in a Cartesian space where x, y, and z are respectively the radial, binornmal (approximately poloidal), and parallel (to B) coordinates. The potential is obtained from a generalized vorticity. SOLT contains a reduced description of the electron drift wave and interchange instabilities, and sheath physics. The latter permits a description of the sheath-driven temperature gradient[14] instability as well as the implementation of sheath boundary conditions on interchange modes. Curvature- and ∇B-driven charge polarization enables transport of enhanced density structures (blobs) with strong fluctuations ($\tilde{n}/n \sim 1$) from the edge into the SOL. The parallel physics is modeled by closure schemes that depend upon the collisionality regime.[15] Other important features of the model are that (i) it does not use the Boussinesq approximation, and (ii) it retains ion temperature effects ($T_i \neq 0$). The first feature is important for blob propagation studies (see Appendix B). The second point is important for H-mode simulations, where the ion diamagnetic drift is often coupled to the $\mathbf{E} \times \mathbf{B}$ drift. Warm ions, which are expected to be present in the edge and SOL region,[16,17] also influence the dynamics of turbulence and blob propagation.[18-23]

In dimensionless form, the SOLT model equations are

$$(\partial_t + \mathbf{v}_E \cdot \nabla)\rho = -2\mathbf{b} \times \kappa \cdot \nabla(p_e + p_i) - \alpha_{sh}J_{\parallel} - A_{dw}(\Phi, n) + \mu\nabla^2\rho - \nu_{\bar{\rho}}\,\bar{\rho} + \frac{1}{2}n\mathbf{v}_{di} \cdot \nabla\nabla^2\Phi$$

$$+ \frac{1}{2}\nabla^2(\mathbf{v}_E \cdot \nabla p_i) - \frac{1}{2}(\mathbf{v}_E \cdot \nabla)\nabla^2 p_i + \frac{1}{2}\mathbf{b} \cdot \nabla v_E^2 \times \nabla n \tag{1}$$

$$(\partial_t + \mathbf{v}_E \cdot \nabla)n = -\alpha_{sh}\Gamma_{\parallel e} + A_{dw}(\Phi, n) + D_n\nabla^2 n + S_n \tag{2}$$

$$(\partial_t + \mathbf{v}_E \cdot \nabla)T_e = -\alpha_{sh}q_{\parallel e}/n + D_{Te}\nabla^2 T_e + S_{Te} \tag{3}$$

$$(\partial_t + \mathbf{v}_E \cdot \nabla)T_i = -\alpha_{sh}q_{\parallel i}/n + D_{Ti}\nabla^2 T_i + S_{Ti} \tag{4}$$

where the generalized vorticity ρ evolved in Eq. (1) is defined by

$$\rho = -\nabla \cdot (n\nabla\Phi + \nabla p_i) \tag{5}$$

The equations are written in dimensionless form using Bohm normalization with reference time-scale $\Omega_{ci}^{-1} = (ZeB/m_i c)^{-1}$ and space-scale $\rho_{sr} = c_{sr}/\Omega_{ci}$, where $c_{sr}^2 = T_{er}/m_i$, and T_{er} is a reference temperature for the normalization. Φ is the electrostatic potential, n is the electron density, $T_{e,i}$ are the electron and ion temperatures, and $p_{e,i} = n\,T_{e,i}$ are the corresponding pressures. The $\mathbf{E} \times \mathbf{B}$ velocity is $\mathbf{v}_E = \mathbf{b} \times \nabla\Phi$, where $\mathbf{b}$ is a unit vector in the magnetic field direction, perpendicular to the plane of the simulations. The ion diamagnetic drift velocity is $\mathbf{v}_{di} = \mathbf{b} \times \nabla p_i/n$. The over-bar, e.g. $\bar{\rho}$ in Eq. (1), denotes the y-average or mean, and we employ the over-tilde to denote fluctuations about the mean.

This edition of the SOLT code differs from previous ones in that it evolves the ion temperature and the generalized vorticity defined in Eq. (5), thus dynamically coupling the ion diamagnetic and $\mathbf{E} \times \mathbf{B}$ drifts. The vorticity evolution (1) is consistent with the drift-ordered, reduced-Braginskii fluid model version derived by Simakov and Catto[24] and is used in the BOUT code.[25] In Eq. (1), the damping of the mean vorticity ($\sim \nu_{\bar{\rho}}\,\bar{\rho}$) provides mean flow damping, e.g. by charge-exchange with neutrals. Note that $\rho = 0$ is satisfied by $\mathbf{v}_E = -\mathbf{v}_{di}$. Thus, to lowest order, flow damping encourages $\bar{v}_{E,y} = -\bar{v}_{di,y}$. The other new terms in Eq. (1) vanish in the limit of zero ion pressure and provide finite Larmor radius (FLR) stabilization. The

last term originates in the convective derivative, $\mathbf{v}_E \cdot \nabla$, acting on $\nabla \cdot (n \nabla \Phi)$ in the generalized vorticity. It is important for describing the Kelvin-Helmholtz (K-H) instability in the presence of a density gradient.

The curvature and grad-B forces combine in the first term ($\sim \kappa \equiv \mathbf{b} \cdot \nabla b$) on the right-hand side of Eq. (1) to drive the interchange instability. In our coordinate system, this term is simply $\beta \, \partial_y(p_e+p_i)$, where $\beta = 2\rho_{sr}/R$ and R is the radius of curvature of the magnetic field ($1/\kappa$), here approximated by the (low field side) major radius of the tokamak. The linearized equations recover the interchange growth rate, $\gamma^2_{mhd} = -\beta \partial_x(p_e + p_i)$, now including the ion pressure contribution.

Thus the main instability drive mechanisms in the model are curvature-interchange, drift wave, Kelvin Helmholtz, and sheath instabilities. The collection of unstable modes grows into a nonlinear quasi-steady saturated state. In general the model permits saturation by wave-breaking (profile modification) and sheared flows. Ion diamagnetism, the generalized (i.e. finite p_i) Reynolds stress in Eq. (1) and the sheath closure conditions, all play a role in determining the radial electric field and the flows, which are free to evolve on the entire simulation domain. The dependence of the saturation levels on the strength of the sheared flows will be discussed in Sec. IV.

The current density $J_{\parallel}$, electron particle flux $\Gamma_{\parallel e}$ and heat fluxes $q_{\parallel e,i}$ in Eqs. (1) - (4) close the system of equations when expressed in terms of Φ, n, T_e and T_i. Those closure relations, valid for a range of collisionality regimes, from conduction-limited (at high collisionality) to sheath-connected, are discussed in Appendix A and in a previous paper that directly motivates the present work.[8] (Expressions given there are slightly modified here to include the ion temperature in the present study.) We emphasize that the current and heat flux adjust continuously between sheath- and conduction-limited expressions in the SOL as the fields evolve, depending self-consistently on the character of the turbulence. Terms proportional to $\alpha_{sh}(x)$ describe losses to the sheath in various collisionality regimes. The operator A_{dw}, which

is proportional to a coefficient α_{dw}, is a model drift-wave operator, also discussed in Appendix A.

The equilibrium profiles vary in the x (radial) dimension in the simulations. The core-side boundary is at x = 0, the separatrix is at x = L_x/2, and the far-SOL boundary is located at x = L_x where L_x is the simulation box size. We also define a local radial coordinate $\Delta x = x - L_x /2$ such that the separatrix is located at $\Delta x = 0$.

The separatrix is modeled by choosing the drift wave and sheath profiles, $\alpha_{dw}(x)$ and $\alpha_{sh}(x)$, properly in each radial region. In the edge region ($\Delta x < 0$), drift-wave physics is retained and the field lines are closed, so $\alpha_{dw}(\Delta x) > 0$ and $\alpha_{sh}(\Delta x) = 0$ throughout this region. In the SOL region ($\Delta x > 0$), the drift-wave contribution is small and the field lines terminate on sheaths, so $\alpha_{sh}(\Delta x) > 0$ and $\alpha_{dw}(\Delta x) = 0$. In this paper, we refer to the boundary between the drift-wave and sheath regions ($\Delta x = 0$) as the "separatrix" even though our 2D model does not have X-point geometry. An example of typical α_{dw} and α_{sh} profiles is shown in Fig. 1 of Ref. 9.

Note that the two-dimensional nature of the SOLT model does not permit a complete treatment of drift-wave physics: only a single dominant $k_\parallel$ mode can be retained which we take to be global in scale: $k_\parallel \sim 1/qR$, where q is a representative value of the safety factor, and R is the major radius. Short scale drift waves have been shown to result in secondary instability and turbulence that dissipates the blob as it propagates across the SOL.[26] Note that the SOLT model does include short scale k_perp modes but, because of the choice $k_\parallel = 0$ in the SOL, any short scale modes there will not be drift waves. Such secondary instability effects from drift waves are represented in the present model by an appropriate choice of D_n as discussed subsequently.

Explicit diffusion coefficients are μ, D_n, D_{Te} and D_{Ti}. These describe diffusive transport processes in addition to that generated self-consistently by drift-interchange turbulence, e.g. neoclassical transport, collisional transport processes due to neutrals, and instabilities outside the scope of the present model. As it is difficult to extract appropriate values for these coefficients from experimental data, we regard them as "free" parameters and adjust them to achieve

physically credible results: they should dissipate the high-k turbulence but not be so large as to dominate the SOL heat flux width or turn off instability. In Sec. III, we describe adjusting the density diffusion coefficient D_n to tune the power P_{SOL} in the simulations to match that observed in the experiments. An exhaustive scan of the free parameters has not been conducted, but we present a physical mechanism responsible for the scalings reported here that is independent of these ad hoc choices.

The sources, S_n, S_{Te}, and S_{Ti}, have the form $S_n = \nu_n(n_0(x)-n)$, etc., which tends to restore the reference profiles ($n_0(x)$, etc.) taken from the experiments. The plasma sources are non-zero only inside the separatrix; evolution in the SOL is source-free, i.e., we assume that recycled neutrals are not ionized in the SOL. The y-averaged values of the sources represent neutral ionization and plasma heating. The sources also maintain profiles against fluctuations, born in the outboard midplane region, with plasma that streams in and out of the midplane region along the closed field lines.

The boundary conditions are as follows. All fluctuations vanish at both x-boundaries. In particular, the electrostatic potential is taken to be constant at both radial boundaries, and these conditions are used to solve Eq. (5) for the potential. At the far-SOL boundary, the constant is $3T_e$, (i.e., ϕ_B see Appendix A), which is consistent with the sheath-limited parallel current that dominates the vorticity evolution in the far-SOL. The inner boundary ($x = 0$) is taken to be sufficiently within the core region ($\Delta x < 0$) and away from the steep-gradients of the edge region that there is no source of turbulence there. The drift-interchange-born fluctuations, considered here, that might propagate back from the edge, where they are born, to this boundary, are absorbed by dissipation in the model. Thus no fluctuations reach the inner boundary in the simulations. The turbulence is homogeneous in the y (bi-orthogonal, approximately poloidal) direction, where periodic boundary conditions are applied.

The goal of this paper is to use the SOLT model to study the edge and SOL turbulence in NSTX for two discharges with and without Li. Although the ion temperature is retained here (and is thought to play a significant role), a detailed study of the effects of ion temperature on

edge turbulence is left to future work. However, the interested reader is referred to Appendix B, where the effects of T_i (and the Boussinesq approximation) are illustrated using seeded blob simulations.

III. SOLT Simulations

A. Experimental Input to SOLT

The parameters and profiles for the simulations are taken from two discharges in NSTX: one without lithium, or "pre-Li", #129015, and one with lithium, or "with-Li", #129038. These discharges are described in Ref. [7] and are two in a series exploring edge turbulence reduction resulting from lithium deposition on plasma-facing components. Both discharges were 0.8 MA H-modes driven by neutral beam injection (NBI). The pre-Li discharge was heated with 3.9 MW NBI, and the with-Li discharge with 2 MW NBI. Despite the difference in injected power, the stored energy was the same in both discharges due to the improved energy confinement that comes with lithium deposition. We fit the density and temperature profiles measured in the experiments with hyperbolic tangent functions, as illustrated in Fig. 1. Simulation profiles relax to these *on the core side of the separatrix* $(\Delta x < 0)$ *only*, at rates that vanish monotonically as the separatrix is approached, i.e. as $\Delta x \to 0^{(-)}$. The dashed lines in the figure indicate that the density and temperatures are increasingly free to evolve as the separatrix is approached and totally unconstrained in the SOL.

The currents and fluxes in Eqs. (1-4) are functions of the turbulence (Φ, n, T_e and T_i) that depend on the fixed parameters of the experiment through the profiles $\alpha_{dw}(x)$ and $\alpha_{sh}(x)$,[8] as discussed in the previous section and in Appendix A. For example, the sheath coefficient $\alpha_{sh}(x)$ is proportional to the inverse connection length from the outer midplane (OM) to the divertor sheath in the SOL. The sheath tends to dominate parallel transport in the SOL as the connection length decreases.
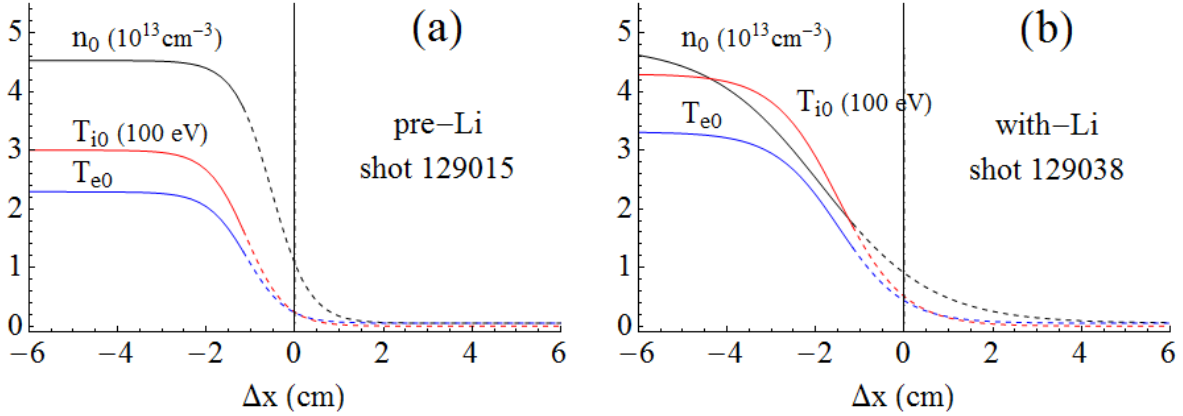
Fig. 1. Reference profiles of density and temperature, relative to the separatrix at $\Delta x = 0$, for (a) the pre-Li discharge (#129015) and (b) the with-Li discharge (# 129038). The solid profiles are constrained to match the experimental data, but the dashed profiles are set by the turbulent transport. Note that the edge gradients are smaller in the case with Li.

B. Matching P_{SOL} to the Experiments

The experimental value of P_{SOL} is taken to be the input NBI power. Ohmic heating, radiation and losses due to charge exchange with neutrals are neglected. For the simulations, P_{SOL} is the radial heat flux ($q_\perp$) at the separatrix, integrated over the poloidal (θ) and toroidal domains. Assuming that there are no heat sources in the SOL and integrating $\nabla \cdot q = 0$ over the SOL ($\Delta x > 0$), we obtain

$$P_{SOL} = \int dA \cdot q_\perp = \int dx\, q_\| 2\pi R B_\theta / B \qquad (6)$$

where we have used $\nabla_\| q_\| = (1/\nu R)\partial q_\| / \partial \theta$ with the local safety factor defined as $\nu = rB/RB_\theta$. Additionally we assume that $q_\perp$ is negligible at the far-SOL boundary. (The factor $2\pi R$ is from the toroidal integral.) Here $q_\|$ is the sum of the electron and ion fluxes, $q_{\|,e}$ and $q_{\|,i}$, indicated in Eqs. (3 and 4) and defined in Appendix A.

Quasi-steady-state turbulence requires a balance of the free energy drives with the dissipation. High-k dissipation is required in the dual cascade to remove vorticity from the

plasma. Since the exact nature of the experimental dissipation is unknown, our simulations use diffusive terms for this purpose. We will show that the ad-hoc diffusion terms do not dominate the transport but do regulate the turbulence.

For reasonable choices of the dissipation parameters $\nu_{\bar{\rho}}$, μ, D_n, D_{Te} and D_{Ti} the SOLT simulations can recover several of the experimental observations. For example, the density diffusion parameter D_n in the simulation can be adjusted to recover the experimentally observed value of P_{SOL}, the power flowing into the SOL. In this figure, the large circles indicate the measured values of P_{SOL}: 3.9 MW in the pre-Li discharge and 2.0 MW in the with-Li discharge. Over the range studied in Fig. 2, P_{SOL} generally decreases with diffusion and is smaller after Li is introduced.
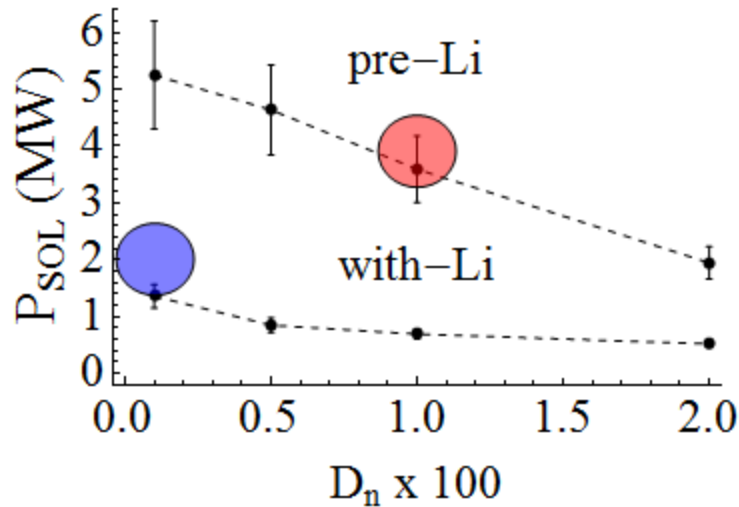

Fig. 2 Power flowing into the SOL, P_{SOL}, from SOLT simulations vs. (100x) the density diffusion coefficient D_n, normalized by the reference Bohm value of 293 m^2/sec. The large circles indicate the intersection of the experimental values of P_{SOL} with the simulation results. The diffusion coefficient in the simulation is chosen to give power-matching to the experiment.
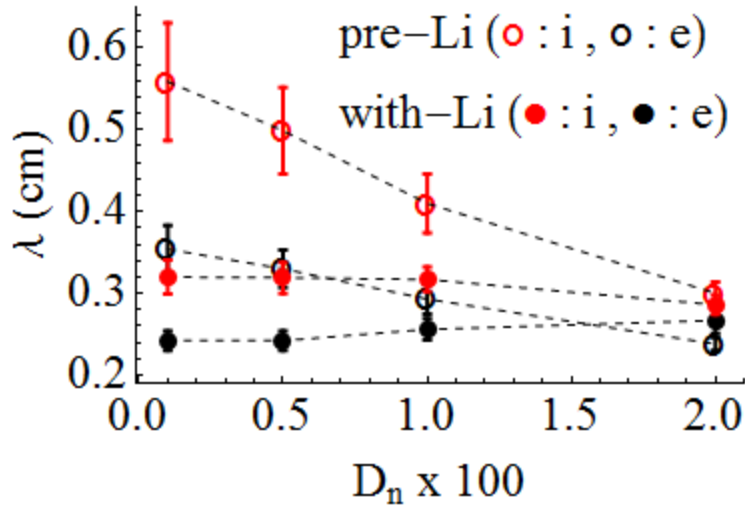
Fig. 3 Simulated heat-flux profile width λ (Eq. 7) in the SOL vs. (100x) the density diffusion coefficient D_n, normalized by the reference Bohm value of 293 m^2/sec, for electrons (black) and ions (red) in the pre-Li (open circle) and with-Li (closed circle) cases. Note the general trend that λ decreases with D_n. Stronger diffusion reduces the turbulent transport and the turbulence-induced flattening of the SOL profiles (giving smaller λ). The values of λ corresponding to power-matching (see Fig. 2) are given in Table 1.

The corresponding heat-flux profile width λ is shown in Fig. 3. Here, we use the Loarte definition[27] of λ (cf. Eq. 6):

$$\lambda = \frac{P_{SOL}}{\left[q_{\parallel}(\Delta x \rightarrow 0) 2\pi R B_{\theta} / B \right]} \tag{7}$$

The electron and ion contributions are shown separately for the pre-Li and with-Li cases. Generally, and in particular for the power-matched cases, the simulated λ is *smaller* for the with-Li case than for the pre-Li case, consistent with the trend observed in experiments. Also note that the width decreases with increasing diffusion coefficient, D_n, particularly in the pre-Li case. If diffusion were driving the heat flux, one would expect λ to increase with increasing D_n, but

the opposite is observed in the simulations: *the turbulence drives the heat flux and the diffusion damps the turbulence*.

Since the simulated heat transport is determined by the turbulence, not the ad hoc dissipation, we can expect the simulation results for pre-Li and with-Li to be physical consquences of the interchange turbulence simulated by the SOLT code. The values of heat-flux profile width obtained in the simulations by power matching is shown in Table 1 for both electrons and ions. This is the main quantitive result of this paper. The remainder of the paper is devoted to obtaining a deeper understanding of the underlying turbulence and the mechanism for turbulent SOL transport.

Table 1. The heat-flux width λ obtained by power-matching the simulation and the experiment, as explained in the text. Results are shown separately for electrons and ions with and without Li.

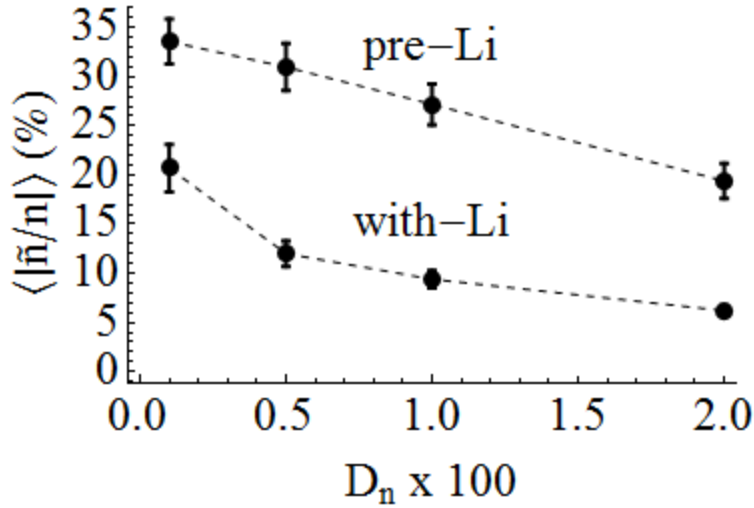| Discharge	Conditioning	Power (MW)	λ_e(cm)	λ_i(cm)
129015	Pre-Li	3.9	0.29	0.41
129038	With-Li	2.0	0.24	0.32

Fig. 4 Simulated turbulent fluctuation amplitudes $\langle|\tilde{n}/n|\rangle$ vs (100x) the density diffusion coefficient D_n, normalized by the reference Bohm value of 293 m^2/sec, for the pre- and with-Li discharges at the radial position $\Delta x = -3$ mm. This figure shows that the use of Li leads to reduced fluctuation amplitudes in the edge, and thus ultimately reduced turbulent transport in the SOL. This conclusion is robust over a wide range of diffusion parameters.

The corresponding density fluctuations in the simulations confirm that the drift-interchange-driven turbulence is *weaker* for the smaller pedestal pressure gradients obtained with Li and stronger for the steeper pre-Li profiles. The resulting fluctuations at $\Delta x = -3$ mm are plotted vs D_n in Fig. 4. The use of Li leads to reduced fluctuation amplitudes (and thus reduced turbulent transport) in the SOL. This conclusion is robust over a wide range of diffusion parameters.

As shown in Fig. 5, the density fluctuations at the separatrix are weaker across the entire wave-number spectrum in the with-Li case. This result is in qualitative agreement with inferences made from modeling of reflectometry measurements.[7] Also note that the peaking at small k in Fig. 5 is typical of drift-interchange turbulence (the inverse cascade). Thus, Figs. 4 and 5 lead to the conclusion that *turbulent heat transport is weaker for the broader pressure profiles with lithium*, as can be expected for a gradient-driven interchange mechanism.
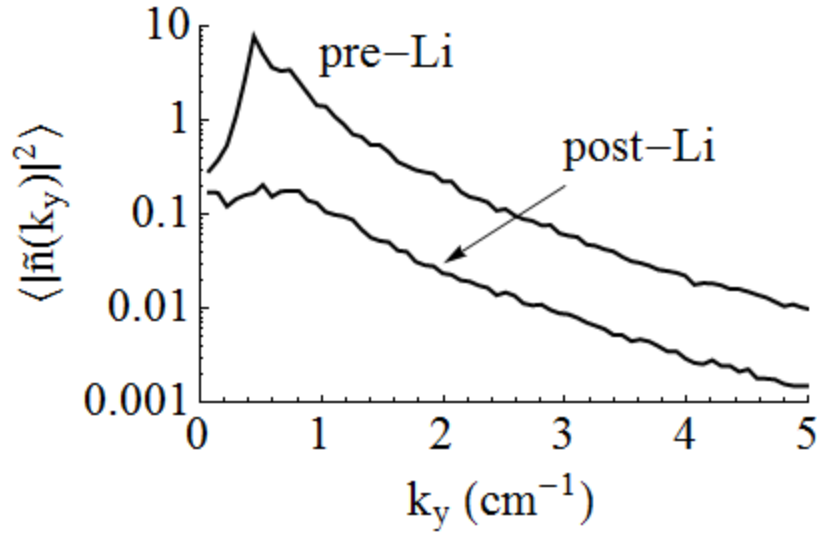
Fig. 5 Simulated turbulent fluctuation spectrum $\langle|\tilde{n}(k_y)|^2\rangle$ vs k_y for the pre- and with-Li discharges at the separatrix ($\Delta x = 0$). This figure shows that density fluctuations are weaker across the wave-number spectrum for the case with Li.

In interpreting these results, we assume that the SOL transport is ultimately caused by turbulent convection of plasma across the field lines due to the local turbulent $\mathbf{E}\times\mathbf{B}$ drifts. However, the local electric field can arise either from local instabilities, or in some circumstances, from instabilities driven at "remote" locations, e.g. due to a type of turbulence spreading. Of interest here, in the latter case, is the emergence of turbulent convection across the separatrix, either in the form of intermittent convective cells, or ejected blob-filaments. In this case, which is called "distributed turbulence" in Ref. 28, there can be an inverse relationship between the pressure gradient scale length λ_p (near the pedestal) and the heat flux width in the SOL ($\lambda_q = \lambda$). The pressure gradient drives the turbulence and determines the heat flux width. In Ref. 28 the following scaling was derived for $\mathbf{E}\times\mathbf{B}$ turbulence using the steady-state power balance equation in the SOL

$$\lambda_q \approx \frac{qR\gamma\,\tilde{v}_x^2}{gc_s|\omega|^2\lambda_p} \tag{8}$$

16

where ω is the frequency and γ is the growth rate of the linear mode, c_s is the sound speed, $\tilde{v}_x^2$ is the saturation level, and in the sheath limited regime, g becomes the sheath energy transmission factor. The other symbols are standard. The important point for the present discussion is that $\lambda_q \propto 1/\lambda_p$.

In the simulations discussed here, the pre-Li case with steep pedestal profiles (small λ_p) was compared to the discharge with Li where the pedestal profiles were much more gentle (large λ_p). Since the simulation profiles were constrained to match the equilibrium profiles inside the separatrix (but not in the SOL!), we essentially specified λ_p for both cases. In qualitative agreement with experimental observations, the simulations show that smaller λ_p in the edge pedestal region corresponds to larger λ_q in the SOL, i.e. the midplane SOL width is largest in the pre-Li discharge and smaller in the with-Li discharge. In SOLT, we interpret the reduced SOL width λ_q as resulting from the more weakly driven turbulence in the large λ_p case. With less turbulence, there is less profile flattening in the SOL and thus smaller λ_q. Thus, the simulation confirms the inverse relationship in Eq. (8) and shows qualitative agreement with the experiment.

IV. Mean Flows in SOLT Turbulence

Sheared mean flows reduce the interchange growth rate and act as transport barriers in the edge region. To the extent that the heat flux width is determined by turbulent transport, as described in the previous section, it is important to explore the mean flows in the simulations and to compare them with those observed in the experiments. If the flows can be modified in the simulation by changing parameters accessible in the experiments, it would have important implications for controlling the turbulent transport and the heat flux width.

The time-averaged mean poloidal flow, $\langle v_{E,y} \rangle$, for the power-matched, pre-Li simulation is shown in Fig. 6. The shape of the profile is generic for these simulations: a near-sonic, positive maximum (in the electron diamagnetic drift direction) inside the separatrix, with flow reversal in the SOL where the sheath enforces the Bohm potential ($3T_e$) and consequent

17

negative (ion diamagnetic direction) flow. Thus there are flow shear layers, $\partial_x <v_{E,y}>$, on either side of the high pressure gradient region, where the ion diamagnetic drift, $<v_{di,y}>$, also plotted in Fig. 6, has a negative global minimum. The maximum magnitude of $<v_{E,y}>$ in the simulations is much larger than the poloidal turbulent structure (blob) velocities observed near the separatrix with GPI on NSTX.[29,30] Poloidal velocities inferred from probe measurements in typical NSTX H-mode discharges are somewhat larger but still well below the magnitudes shown in Fig. 6.[31] This raises the question of how blobs move in the presence of background flows.
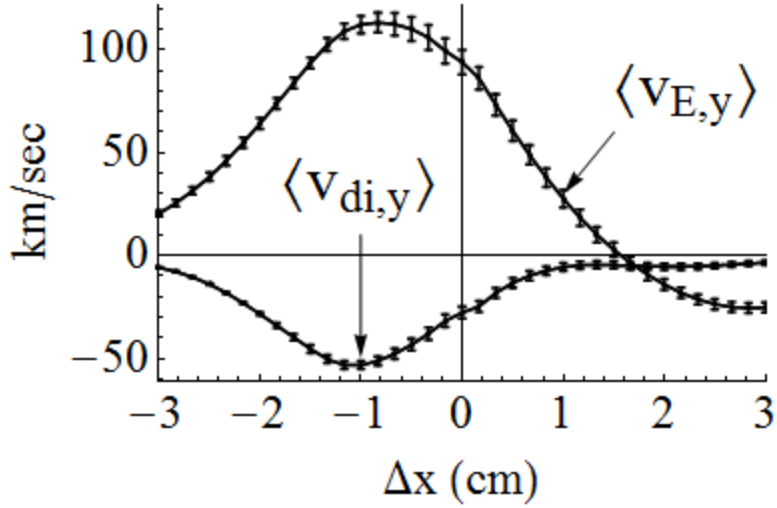

Fig. 6. Poloidal E×B and ion diamagnetic drift velocities ($v_{E,y}$ and $v_{di,y}$, respectively) averaged over the poloidal dimension (y) and time for the power-matched pre-Li simulation. Error bars are standard deviations.

To explore this question, we introduce a synthetic structure velocity for the simulations. Near the separatrix, blob density tracks in (y,t) space show up as strong linear features in the power spectrum of the density fluctuations. Thus, at each radial location (Δx), we define the *structure velocity* to be the phase velocity at the global maximum of the power spectrum, $|\tilde{n}(\Delta x, k_y, \omega)|^2$. This definition gives the solid black line in Fig. 7.
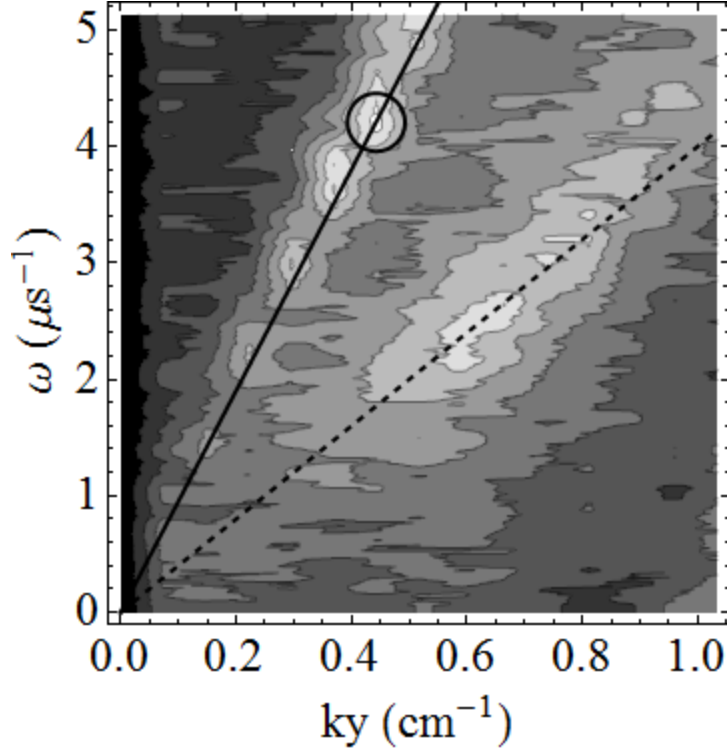
Fig. 7. The definition of the synthetic structure velocity, based on the density fluctuation spectrum $\left|\tilde{n}(\Delta x, k_y, \omega)\right|^2$ is illustrated at the separatrix ($\Delta x = 0$). At each Δx, the structure velocity is defined as the phase velocity at the power maximum (circled), typically associated with a relatively narrow resonance (solid line). A broader resonance, which also exhibits a characteristic velocity (dashed line), is associated with a subdominant mode.

When this velocity is plotted as a function of Δx, it is seen to be constant on radial intervals (see Fig. 8). One such interval includes the pedestal region and overlaps the separatrix, extending into the near-SOL, while another starts near the flow-reversal point and extends into the far-SOL. Linear analysis of the time-averaged turbulence profiles reveals distinct normal modes localized to these radial zones. Interestingly, phase velocities constant in distinct radial zones and exhibiting jumps near the separatrix were also seen in an analysis of GPI data on Alcator C-Mod.[32] From this we conclude that in SOLT, *modes localized to radial zones underlie the turbulence*.
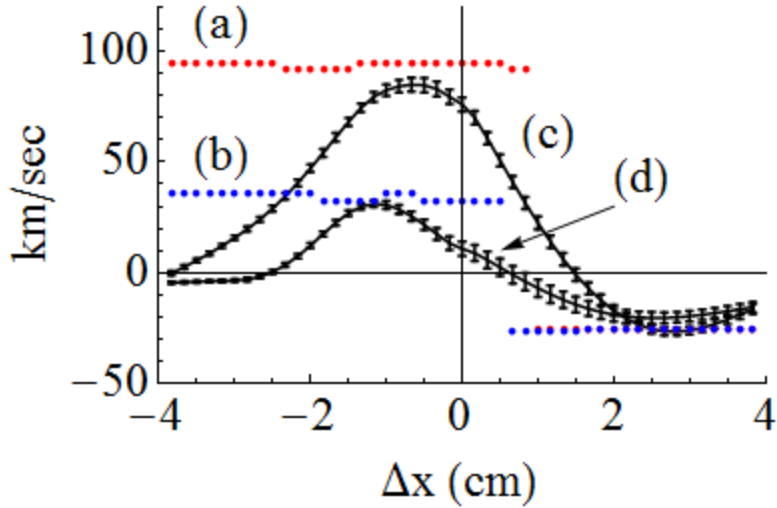
Fig. 8. The structure velocity in the pre-Li simulations without (a, red) and with (b, blue) flow damping, constant on radial zones, reveals underlying radial eigenmodes. The group velocity profile $\langle v_{E,y}\rangle + \frac{1}{2}\langle v_{di,y}\rangle$ (black) is shown for comparison: without (c) and with (d) flow damping.

Several features in Fig. 8 are notable. One is that the observed structure velocities tend to lock on to values at the extrema of the profile function $\langle v_{E,y} + v_{di,y}/2\rangle$. These points are near the locations of the minimum velocity-shearing rate. We speculate that the modes center themselves at these locations, since they are most favorable to robust linear growth. Next we explore the question of why the profile of significance is $\langle v_{E,y} + v_{di,y}/2\rangle$.

There are several characteristic velocities which enter the theory: v_E is the lowest order guiding center velocity and the perpendicular convection velocity for particles and heat; $v = v_E + v_{di}$ is the total ion fluid flow velocity, i.e. the velocity appearing in lowest order force balance, $n_i Ze(\mathbf{E}+\mathbf{v}\times\mathbf{B}/c) = \nabla p_i$. As we show in the following, under reasonable assumptions, $v_{E,y} + v_{di,y}/2$ is the group velocity of an interchange mode, and finally there is the structure velocity defined in Fig. 7, which may be related to the poloidal blob propagation speed. To understand the group velocity better, consider the well-known dispersion relation for linear waves in a plasma with finite Larmor radius (FLR) effects[33]

$$\tilde{\omega}(\tilde{\omega}-\omega_{*i})+\gamma^2_{mhd}=0 \quad , \tag{9}$$

where $\tilde{\omega} = \omega - k_y v_{Ey}$ is the frequency in the E×B drift frame, $\omega_{*i} = k_y c_s \rho_s / \lambda_{pi}$, $\tilde{\omega}\omega_{*i}$ is the FLR stabilization term, and $\gamma_{mhd} \approx c_s/(R\lambda_p)^{1/2}$ is the interchange mode growth rate. In the limit $\gamma_{mhd} >> \omega_{*i}$, we solve the quadratic equation (8) to obtain the following expression for the phase and group velocity:

$$v_g \equiv d\omega/dk_y = v_{E,y} + v_{di,y}/2 \tag{10}$$

which gives the black curves in Fig. 8. Thus, for the simulations discussed here, the structure velocity of the separatrix-spanning turbulence is nearly given by the phase and group velocity of an ion-diamagnetic-modified interchange mode, in the local approximation to the dispersion relation. The correspondence between the structure velocity and the group or phase velocity is expected for small perturbations; it is not at all clear it should hold in the nonlinear regime. The issue of understanding turbulent structure velocities in general remains a topic of ongoing investigation.

Figure 8 also shows that in the absence of flow damping the maximum structure velocity is of order 100 km/s in the pedestal region, which is much larger than the structure velocity measured by the GPI[29,30] (1 − 5 km/s) for a wide range of NSTX discharges including ones similar to the present pre-Li case. But, with the flow damping parameter ($v_{\bar{\rho}}$, cf. Eq. 1) greater than zero, the computed value of the structure velocity at the separatrix decreases to 32 km/sec, while the far-SOL velocity remains at (−) 6 km/sec (at the limiter entrance). So at least in the pre-Li case, where we studied this effect, flow damping is able to bring the simulation velocities closer to the experimentally measured values. This observation motivated us to investigate the effect of flow damping on the power budgets in the pre-Li and with-Li discharges, as shown in Fig. 9.

Plotted in Fig. 9 is the heat flux (P_{SOL}) versus the damping parameter $v_{\bar{\rho}}$ for vorticity. This parameter also strongly affects the flow shear. In the pre-Li curve, there is a transition from the weak damping (low $v_{\bar{\rho}}$) regime, where the sheared flow is strong and suppresses the turbulence, to a strong-damping (high $v_{\bar{\rho}}$) regime where the flows are too weak to control the

turbulence and the saturation is due to profile flattening (wave breaking) instead of sheared-flow stabilization.[9] In general, simulations show that as flow damping increases, and flow shear decreases, turbulent saturation levels rise, until they plateau in the wave-breaking regime. In the with-Li case, the profiles are so relaxed that the flows are weak and the damping is unimportant: saturation at wave-breaking levels is still small.

The physical origin of flow damping is not yet clear. Neutral friction provides one possibility; however, if typical NSTX midplane values of neutral density[34] are employed, the friction is too small to account for the values of $\nu_{\bar{\rho}}$ explored here. It is possible that zonal and mean flows (being poloidally symmetric) could be affected by the much larger neutral density expected in the divertor and X-point region, but neutral measurements in the X-point region are not available at present.

The relationship of edge neutral density to poloidal flow velocity is also discussed in Ref. 29 where, in similar discharges, a slight but systematic increase in the poloidal velocity with Li deposition was observed. Li is generally thought to reduce edge recycling and hence edge neutral density and the resulting neutral friction. This could in principle provide a mechanism for the changes in poloidal flows observed in that work. This same mechanism might be related to the need for flow damping in the pre-Li simulation in order to obtain better agreement with experimental structure velocities.

Finally, note that flow damping raises the heat exhaust for the pre-Li profiles and thereby increases the interaction of the plasma with the wall. It also imposes the profile constraint $\langle v_{E,y} \rangle \rightarrow -\langle v_{di,y} \rangle$ as $\nu_{\bar{\rho}} \rightarrow \infty$ (cf. Eq. 5).
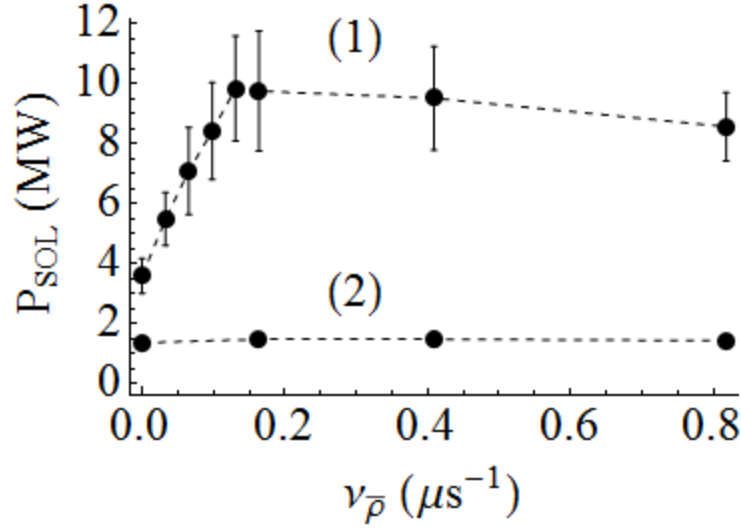
Fig. 9. Plots of the SOL heat flux P_{SOL} vs the damping parameter $\nu_{\bar{\rho}}$ are shown for (1) the pre-Li discharge and (2) the with-Li discharge. The input density and temperature profiles inside the separatrix are steep for the pre-Li case and gentle in the with-Li case.

V. Summary and Conclusions

In this paper SOLT simulations have been compared with experiments on NSTX with and without lithium deposition. One goal was to explore the nature of the interchange turbulence using Li to modify the pressure profiles which drive the turbulence. A second goal was to see whether the relatively simple SOLT 2D turbulence model could reproduce the experimental trends, and whether the trends observed in the SOL heat flux width may be attributed to turbulent transport.

The main conclusions of our study are as follows:

(1) When the simulated power flowing into the SOL, P_{SOL}, is adjusted to match that of the experiment, we find that the SOL heat-flux widths are *smaller* for the gentler pressure profiles that result from lithium deposition, and *larger* for the steeper pre-lithium profiles. This trend agrees with experiment.[6] See Fig. 3 and Table 1. The apparent explanation for this trend,

derived from these simulations, is that turbulent transport generated in the lower pedestal region drives the heat flux and heat flux width in the SOL. This is an example of "distributed turbulence" and has the property that the scale lengths for the pressure gradient and the SOL heat flux are *inversely related.*[28] This relationship and turbulence regime, applicable, we argue, to lithiated H-modes in NSTX, is not universal, i.e. independent of other conditions. For example, cooler low confinement (L) mode plasmas, are expected to be unstable to quasi-local resistive instabilities, resulting in a different transport scaling for the SOL width.[28] The inverse scaling of pedestal and SOL widths for NSTX H-mode plasmas is an important conceptual point and it will be important to understand its generality in future investigations. Although the computed SOL heat flux widths do not agree quantitatively with the experimental ones for this discharge, they are consistent with the range in the experimental database (pre-Li: 4 – 15 mm; with-Li: 2 – 6 mm) for similar discharges, in particular discharges at the same value of plasma current I_p.

(2) The simulated density fluctuations with Li at the separatrix are weaker across the spectrum than pre-Li fluctuations, in qualitative agreement with inferences from reflectometry measurements.[7] See Figs. 4 and 5.

(3) Modes localized to radial zones underlie the turbulence. The simulated structure velocity near the separatrix is approximately $\langle v_{E,y} \rangle + \frac{1}{2} \langle v_{di,y} \rangle$, as expected of interchange modes modified by ion diamagnetic effects. The phase velocity locks on to the values at the extrema of this phase and group velocity profile where the velocity shear is weak. See Fig. 8.

(4) Flow damping reduces the SOLT structure velocities (see Fig. 9), as required for agreement with GPI observations. However, very strong flow damping would be required to obtain values close to the GPI observations on similar discharges, and the physical mechanism is not apparent.

Concerning the observed and simulated narrowing of the heat flux width with lithium, one might naively expect that the peak power on the divertor would go up with Li because when the SOL heat flux width λ_q is reduced, the power could be concentrated in a narrower channel to the divertor plates. However, this is not the case: in the NSTX experiments[6] the peak power

on the divertor was observed to decrease with Li, making the net effect of Li beneficial. There are a number of effects outside the scope of our midplane turbulence model which might account for this effect, including divertor leg turbulence, and radiative and other dissipative power losses, resulting from changes in the divertor conditions with Li.

One area in which the simulations could be improved is in reconciling the measured and simulated poloidal velocities and in understanding the damping mechanisms. An important topic for future studies is the possible interplay between neutral recycling, flow damping by neutrals, and its impact on the heat flux width. Other mechanisms that could affect the velocities near the separatrix include neoclassical orbit effects, ion X-point losses or other viscous damping.

Acknowledgements

Appendix A: Parallel closures

The SOLT simulation model has been discussed in several recent papers.[8,9,35] Here, we summarize the parallel closures used in the present version of the 2D SOLT model that includes, for the first time, the finite ion pressure terms.

Analytical closure relations are employed to describe the parallel dynamics. For example, the relationship of parallel current $J_\parallel$ to Φ is prescribed by a sheath closure on open field lines (generalized to allow for collision-dominated regimes), and a Wakatani-Hasegawa-like model[36] for $J_\parallel$ is employed on closed field lines to capture basic drift-wave physics.

The fundamental equations for the SOLT model are the vorticity, continuity and temperature equations, as presented in Eqs. (1) – (4). In these equations, the drift wave operator A_{dw} and *drift wave parameter* α_{dw} are defined by

$$A_{dw}(\phi, n) = \alpha_{dw}\overline{T}^{3/2}\{\phi - T\ln n\} \tag{A1}$$

$$\alpha_{dw} = \frac{2k_{\parallel}^2 v_{te}^2}{\nu_{ei}\Omega_i} \tag{A2}$$

where $<Q> \equiv \overline{Q}$ denotes the zonal or y-averaged part and $\tilde{Q} \equiv \{Q\} \equiv Q - \overline{Q}$ denotes the fluctuating part for any quantity Q. Thus, A_{dw} enforces a Boltzmann response on fluctuations when the coefficient α_{dw} is large, in the spirit of the Wakatani-Hasegawa adiabaticity parameter. Note that the flux-surface or y-average of A_{dw} vanishes (as it must since it arises from $\nabla_{\parallel}J_{\parallel}$ on closed surfaces).

It remains to describe the closure relations for $J_{\parallel}$, $\Gamma_{\parallel e}$, $q_{\parallel e,i}$ in terms of Φ, n, T_e and T_i. In the respective governing equations, these parallel fluxes are multiplied by a dimensionless characterization of the field line connection length in the SOL, the *sheath conductivity parameter*

$$\alpha_{sh} = \frac{\rho_{sr}}{L_{\parallel}} \tag{A3}$$

where $L_{\parallel}$ is the midplane-to-divertor-plate connection length in the SOL and ρ_{sr} is the reference sound gyro-radius. The parallel current and heat fluxes are given (in dimensionless Bohm units) by

$$J_{\parallel SL} = n(T_e + \gamma T_i)^{1/2}\left(1 - e^{(\phi_B - \phi)/T}\right) \tag{A4}$$

$$q_{\parallel eSL} = s_E\, nT_e(T_e + \gamma T_i)^{1/2}e^{(\phi_B - \phi)/T} \tag{A5}$$

$$q_{\parallel i} = nT_i(T_e + \gamma T_i)^{1/2} \tag{A6}$$

and the parallel electron particle flux is

$$\Gamma_{\parallel e} = n(T_e + \gamma T_i)^{1/2} - J_{\parallel} \tag{A7}$$

where Φ_B is the Bohm potential at the sheath, γ is the ratio of specific heats and s_E is the sheath energy transmission factor. In the simulations of this paper we take $\Phi_B = 3T_e$, $\gamma = 1$ and $s_E = 6$. Here SL refers to the sheath-connected limit (SL).

To account for parameter regimes in which the electrons are more collisional, and hence not sheath limited, we define the following conduction-limited closure relations[8]

$$J_{||eCL} = -\frac{1.96nT_e^{1/2}}{\Lambda}\frac{(\Phi_B - \Phi)}{T_e} \tag{A8}$$

$$q_{||eCL} = \frac{3.2nT_e^{3/2}}{\Lambda} \tag{A9}$$

where the collisionality parameter Λ is given by

$$\Lambda = \frac{\nu_{ei}L_{||}}{\Omega_e\rho_s} \tag{A10}$$

The parameter Λ is related to the SOL electron collisionality parameter $\nu_{*e} = L_{||}/\lambda_{ei} = \Lambda(m_i/m_e)^{1/2}$, where λ_{ei} is the electron mean free path for collisions with ions. For intermediate cases, these parallel closures are interpolated to provide a smooth connection between the sheath and conduction limited regimes. Flux limits are also imposed. Clearly the replacement of parallel gradient operators by $1/L_{||}$, implicit in these definitions, limits the quantitative accuracy of the model. Nevertheless, it is expected that the model will be faithful in describing major qualitative trends with collisionality, as already demonstrated in previous work.[9]

Appendix B: Effect of finite T_i on blob propagation

One simple demonstration of the finite ion temperature model is to study its effect on seeded blob motion. In agreement with similar seeded blob studies,[18,19,22] we show here that finite T_i enhances the coherence of the blobs and increases their radial motion.

Finite ion temperature enters blob physics in several ways. [20,37] First, ion pressure contributes to the interchange-curvature drive, viz. the radial curvature "force" $F \sim nm_ic_s^2/R$

27

$\propto (T_e + T_i)/R$. This enhances the radial blob motion (and increases the interchange drive for turbulence). Second, in the Bohm sheath condition, which enters through $J_{||}$ in the vorticity equation (1), the ion flux at the sheath entrance must be generalized[38] to include the T_i dependence of $c_s \sim (T_e + \gamma_s T_i)^{1/2}/m_i^{1/2}$ as indicated in Appendix A. Finally, there are additional terms in the vorticity equation representing ion polarization currents due to finite ion Larmor radius and gyro-viscous physics.

Figure 10 shows a comparison of seeded blob simulations for three values of the dimensionless ion temperature. For each T_i, two simulations are shown: the lower one uses the Boussinesq approximation (BA) and the upper one solves the full problem using a multi-grid (MG) method.

Recall that the BA consists of taking the density to be constant in the vorticity ρ. Until recently this was a standard approximation in most turbulence codes primarily because it has the desirable effect of reducing Eq. (5) to a relatively fast Poisson-solve for the potential Φ. But in the edge region, where the density gradients of the mean field and of the fluctuations are not defensibly ignored, this is a poor approximation. Abandoning the BA means solving the more general and numerically time-consuming equation, typically either by direct methods (e.g. bi-conjugate gradient[39]) or by relaxation methods.[40,41] Reference 41 introduces an iterative method for solving the non-Boussinesq equation (5) that makes important use of an acceleration parameter. (Unfortunately, this technique was not available when the present research was conducted, though it has since been incorporated into SOLT.)

The MG method[42] offers the possibility of accelerating convergence in relaxation methods of solving Eq. (5), achieving acceptably accurate solutions in record time. The method exploits the fact that numerical errors are quickly removed (by numerical diffusion) by relaxation at shorter spatial scales but linger at longer scales. So the equation is projected onto a sequence of progressively coarser grids where relaxation on the n-th grid reduces the error at long scales lingering on the (n-1)-st grid that show up at intermediate scales on the n-th grid. The exact solution for the error is obtained on the coarsest grid by direct solution (by the bi-conjugate

gradient method here) and the corrected solution is interpolated back to the original (finest) grid. The method can reach a prescribed error tolerance faster than relaxation alone on the original (finest) grid in some cases. However, the convergence properties of relaxation methods and their MG enhancements depend crucially on the character of the density fluctuations that enter the *non-Boussinesq* vorticity equation (5). For given density fluctuations it may be possible to tune the relaxation and interpolation parameters to optimize convergence, but we know of no general rule for doing so that would be useful in a *turbulent* setting where the fluctuations are not constrained *ab initio* and change unpredictably from time step to time step. Our success with the method is based on trial-and-error.

The results of the seeded blob study (obtained using the MG method and 3 coarse grids) show that the ion pressure enhances the curvature-drive and thus both the radial motion and the secondary instability of the blobs. Compared to the general case, Boussinesq blobs are unstable to secondary instabilities and liable to underestimate turbulent transport in blob simulations. This is shown in dramatic fashion by the computed blob tracks shown in Fig. 11. For purposes of both verification and illustration, rather extreme parameter values were chosen for these cases. It has been noted previously that the BA has a similar effect in cold ($T_i = 0$) models.[43] In both cases, finite T_i terms break the bi-normal (y) symmetry and result in induced poloidal motion.[18,19]

Thus, we find that retaining finite ion temperature can have a significant effect on blob motion. In the main body of the paper, we retained T_i in the Li turbulence studies. The solution of Eq. (5) was by relaxation on three or fewer coarse grids. The parameters of the method were chosen to achieve convergence with iteration and reduction of the residual error to a prescribed tolerance. Failing convergence and error-reduction at any given time step, the solution was obtained by the bi-conjugate gradient method on the original grid. We regard the MG method as holding great promise for our problem. But further analysis and numerical experimentation are required before it can be regarded as a robust tool for exploring edge turbulence.
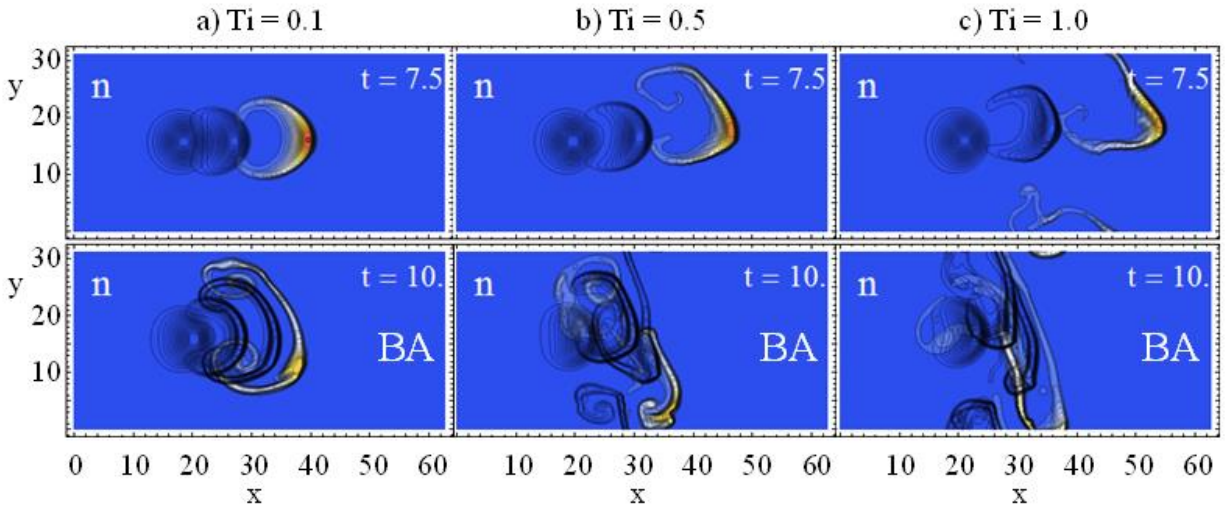
Fig. 10. Comparison of seeded blob simulations for dimensionless $T_i = 0.1$, 0.5 and 1.0 with (upper) and without (lower) the Boussinesq approximation (BA). The other parameters are $n_0 = 0.05$, $T_e = 1$, $\beta = 1$ in the dimensionless Bohm units of Eqs. (1-5).
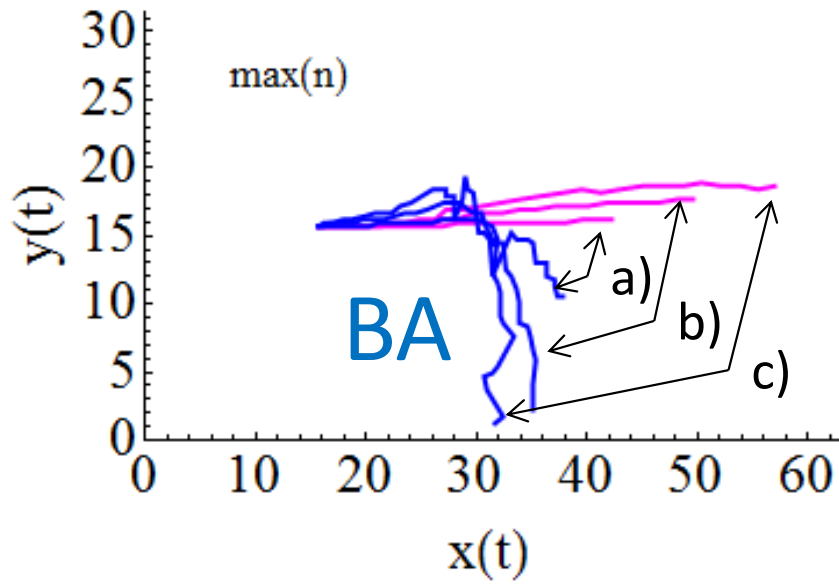

Fig. 11. Blob trails corresponding to the simulations of Fig. 10.

References

[1] H. W. Kugel, M. G. Bell, J.-W. Ahn, J. P. Allain, R. Bell, J. Boedo, C. Bush, D. Gates, T. Gray, S. Kaye, R. Kaita, B. LeBlanc, R. Maingi, R. Majeski, D. Mansfield, J. Menard, D. Mueller, M. Ono, S. Paul, R. Raman, A. L. Roquemore, P. W. Ross, S. Sabbagh, H. Schneider, C. H. Skinner, V. Soukhanovskii, T. Stevenson, J. Timberlake, W. R. Wampler, L. Zakharov, Phys. Plasmas **18**, 056118 (2008).

[2] M. G. Bell, H. W. Kugel, R. Kaita, L. E. Zakharov, H. Schneider, B. P. LeBlanc, D. Mansfield, R. E. Bell, R. Maingi, S. Ding, S. M. Kaye, S. F. Paul, S. P. Gerhardt, J. M. Canik, J. C. Hosea, G. Taylor, and the NSTX Research Team, Plasma Phys. Controlled Fusion **51**, 124054 (2009).

[3] J. M. Canik, W. Guttenfelder, R. Maingi, T.H. Osborne, S. Kubota, Y. Ren, R.E. Bell, H.W. Kugel, B.P. LeBlanc and V.A. Souhkanovskii, Nucl. Fusion **53**, 113016 (2013).

[4] R. Maingi, T. H. Osborne, B. P. LeBlanc, R. E. Bell, J. Manickam, P. B. Snyder, J. E. Menard, D. K. Man, H. W. Kugel, R. Kaita, S. P. Gerhardt, S. A. Sabbagh, F. A. Kelly, and the NSTX Research Team, Phys. Rev. Lett. **103**, 075001 (2009).

[5] R. Maingi, D.P. Boyle, J.M. Canik, S.M. Kaye, C.H. Skinner, J.P. Allain, M.G. Bell, R.E. Bell, S.P. Gerhardt, T.K. Gray, M.A. Jaworski, R. Kaita, H.W. Kugel, B.P. LeBlanc, J. Manickam, D.K. Mansfield, J.E. Menard, T.H. Osborne, R. Raman, A.L. Roquemore, S.A. Sabbagh, P.B. Snyder and V.A. Soukhanovskii, Nucl. Fusion **52**, 083001 (2012).

[6] T.K. Gray, J.M. Canik, R. Maingi, A.G. McLean, J-W. Ahn, M.A. Jaworski, R. Kaita, M. Ono, S.F. Paul and the NSTX Team, Nucl. Fusion **54**, 023001 (2014).

[7] J. M. Canik, R. Maingi, S. Kubota, Y. Ren R. E. Bell, J. D. Callen, W. Guttenfelder, H. W. Kugel, B. P. LeBlanc, T. H. Osborne, and V. A. Soukhanovskii, Phys. Plasmas **18**, 056118 (2011).

[8] J. R. Myra, D. A. Russell, D. A. D'Ippolito, J-W. Ahn, R. Maingi, R. J. Maqueda, D. P. Lundberg, D. P. Stotler, S. J. Zweben, J. Boedo, M. Umansky and NSTX Team, Phys. Plasmas **18**, 012305 (2011).

[9] D. A. Russell, D. A. D'Ippolito, J. R. Myra, B. LaBombard, J. L. Terry, and S. J. Zweben Phys. Plasmas **19**, 082311 (2009).

[10] F. Militello, V. Naulin, and A.H. Nielsen, Plasma Physics and Controlled Fusion **55**, 074010 (2013).

[11] F. D. Halpern, P. Ricci, S. Jolliet, J. Loizu, and A. Mosetto, Nuclear Fusion **54**, 043003,(2014).

[12] A. Mosetto, F. D. Halpern, S. Jolliet, J. Loizu, and P. Ricci, Phys. Plasmas **20**, 092308 (2013).

[13] C. S. Chang, J. A. Boedo, R. Hager, S.-H. Ku, J. Lang, R. Maingi, D. Stotler, S. Zweben, and S. Parker, 25th IAEA Fusion Energy Conference, Saint Petersburg, Russia, October 13 - 18, 2014, paper IAEA-CN-221/TH/2-3.

[14] H. L. Berk, R. H. Cohen, D. D. Ryutov, Yu. A. Tsidulko, and X. Q. Xu, Nucl. Fusion **33**, 263 (1993).

[15] S. I. Krasheninnikov, D. A. D'Ippolito and J. R. Myra, J. Plasma Phys. **74**, 679 (2008).

[16] G. Birkenmeier, F. M. Laggner, M. Willensdorfer, T. Kobayashi, P. Manz, E. Wolfrum, D. Carralero, R. Fischer, B. Sieglin, G. Fuchert, U. Stroth and the ASDEX upgrade team, Plasma Phys. Control. Fusion **56**, 075019 (2014).

[17] P. Manz, G. Birkenmeier, D. Carralero, G. Fuchert, H. W. Müller, S. H. Müller, B. D. Scott, U. Stroth, T. T. Ribeiro, E. Wolfrum and the ASDEX Upgrade Team, Plasma Phys. Control. Fusion **57**, 014012 (2015).

[18] D. Jovanovic, P. K. Shukla and F. Pegorano, Phys. Plasmas **15**, 112305 (2008).

[19] J. Madsen, O. E. Garcia, J. S. Larsen, V. Naulin, A. H. Nielsen and J. J. Rasmussen Phys. Plasmas **18**, 112504 (2011).

[20] P. Manz, D. Carralero, G. Birkenmeier, H. W. Müller, S. H. Müller, G. Fuchert, B. D. Scott, and U. Stroth, Physics of Plasmas **20**, 102307 (2013).

[21] N. Bisai and P. K. Kaw, Phys. Plasmas **20**, 042509 (2013).

[22] M. Wiesenberger, J. Madsen, and A. Kendl, Physics of Plasmas **21**, 092301 (2014).

[23] A. Mosetto, F. D. Halpern, S. Jolliet, J. Loizu, and P. Ricci, Physics of Plasmas **22**, 012308 (2015).

[24] A.N. Simakov and P.J. Catto, Phys. Plasmas **10**, 4744 (2003).

[25] M.V. Umansky, X.Q. Xu, B. Dudson, L.L. LoDestro and J.R. Myra, Comp. Phys. Comm. **180**, 887 (2009).

[26] J.R. Angus, S.I. Krasheninnikov and M.V. Umansky, Phys. Plasmas **19,** 082312 (2012).

[27] A. Loarte, S. Bosch, A. Chankin, S. Clement, A. Herrmann, D. Hill, K. Itami, J. Lingertat, B. Lipschultz, K. McCormick, R. Monk, G.D. Porter, M. Shimada and M. Sugihara, J. Nucl. Mater., **266-269**, 587-592 (1999).

[28] J. R. Myra, D. A. D'Ippolito and D. A. Russell, Phys. Plasmas **22**, 042516 (2015).

[29] B. Cao, S. J. Zweben, D. P. Stotler, M. Bell, A. Diallo, S. M. Kaye and B. LeBlanc, Plasma Phys. Control. Fusion **54**, 112001 (2012).

[30] S.J. Zweben, W.M. Davis, S.M. Kaye, J.R. Myra, R.E. Bell, B.P LeBlanc, R.J. Maqueda, T. Munsat, S.A. Sabbagh, Y. Sechrest, D.P. Stotler and the NSTX Team, submitted to Nucl. Fusion (2015).

[31] J. A. Boedo, J. R. Myra, S. Zweben, R. Maingi, R. J. Maqueda, V. A. Soukhanovskii, J. W. Ahn, J. Canik, N. Crocker, D. A. D'Ippolito, R. Bell, H. Kugel, B. Leblanc, L. A. Roquemore, D. L. Rudakov, and NSTX Team, Phys. Plasmas **21**, 042309 (2014).

[32] I. Cziegler, J. L. Terry, J. W. Hughes, and B. LaBombard, Phys. Plasmas **17**, 056120 (2010).

[33] W.M. Tang and P.J. Catto, Phys. Fluids **24**, 1314 (1980).

[34] D. P. Stotler, F. Scotti, R. E. Bell, B. P. LeBlanc and R. Raman, submitted to J. Nucl. Mater. (2014); doi: 10.1016/j.nucmat.2014.11.097.

[35] J. R. Myra, W.M. Davis, D. A. D'Ippolito, B. LaBombard, D. A. Russell, J.L. Terry, and S. J. Zweben, Nucl. Fusion **53**, 073013 (2013).

[36] M. Wakatani and A. Hasegawa, Phys. Fluids 27, 611 (1984).

[37] D.A. D'Ippolito, J.R. Myra and S.J. Zweben, Phys. Plasmas **18**, 060501 (2011).

[38] Peter C. Stangeby, *The Plasma Boundary of Magnetic Fusion Devices*, (Institute of Physics Publishing, Bristol and Philadelphia, PA, 2000).

[39] W.H. Press, S.A. Teukolsky, W.T. Vetterling and B.P. Flannery, *Numerical Recipes in Fortran 77 : The Art of Scientific Computing*, 2nd ed., Cambridge University Press (1992), Sec. 2.7, pg. 77.

[40] Ibid, Sec. 19.5, pg. 854.

[41] J.R. Angus and M.V. Umansky, Phys. Plasmas **21**, 012514 (2014).

[42] W.L. Briggs, V.E. Henson and S.F. McCormick, *A Multigrid Tutorial*, 2nd ed., Society for Industrial and Applied Mathematics (2000); D.A. Russell, D.A. D'Ippolito and J.R. Myra, Bull. Am. Phys. Soc., Series II, 57, No. 12 (2012), Session BP8, Poster 159.

[43] G. Q. Yu, S. I. Krasheninnikov, and P. N. Guzdar, Phys. Plasmas **13**, 042508 (2006).